

Relative observing speed of lens-coupled absorber focal plane arrays for far-IR imaging and spectroscopy a PRIMA case study

van Berkel, Sven; Dabironezare, Shahab Oddin; Chattopadhyay, Goutam; Foote, Marc; Glenn, Jason; Baselmans, Jochem; Bradford, Charles

DOI

10.1117/1.JATIS.11.3.031613

Publication date 2025

Document VersionFinal published version

Published in

Journal of Astronomical Telescopes, Instruments, and Systems

Citation (APA)

van Berkel, S., Dabironezare, S. O., Chattopadhyay, G., Foote, M., Glenn, J., Baselmans, J., & Bradford, C. (2025). Relative observing speed of lens-coupled absorber focal plane arrays for far-IR imaging and spectroscopy: a PRIMA case study. *Journal of Astronomical Telescopes, Instruments, and Systems*, *11*(3), Article 031613. https://doi.org/10.1117/1.JATIS.11.3.031613

Important note

To cite this publication, please use the final published version (if applicable). Please check the document version above.

Copyright

Other than for strictly personal use, it is not permitted to download, forward or distribute the text or part of it, without the consent of the author(s) and/or copyright holder(s), unless the work is under an open content license such as Creative Commons.

Takedown policy

Please contact us and provide details if you believe this document breaches copyrights. We will remove access to the work immediately and investigate your claim.



RESEARCH PAPER

Relative observing speed of lens-coupled absorber focal plane arrays for far-IR imaging and spectroscopy: a PRIMA case study

Sven van Berkelo, a,* Shahab Oddin Dabironezareo, b,c Goutam Chattopadhyay, a Marc Foote, a Jason Glenno, d Jochem Baselmanso, b,c and Charles Bradforda ^aCalifornia Institute of Technology, NASA Jet Propulsion Laboratory, Pasadena, California, United States ^bSRON-Netherlands Institute for Space Research, Leiden, The Netherlands ^cDelft University of Technology, Faculty of Electrical Engineering, Mathematics and Computer Science, Delft, The Netherlands

^dNASA Goddard Space Flight Center, Greenbelt, Maryland, United States

ABSTRACT. The PRobe far-Infrared Mission for Astrophysics (PRIMA) is an astrophysics mission concept currently under study. The instrument comprises four focal plane arrays (FPAs), each with over 1000 pixels, consisting of lens-coupled kinetic inductance detectors designed for ultra-high sensitivity spectroscopy and imaging. PRIMA covers the far-infrared band from 24 to 250 μ m. We present the fundamental properties of lens-coupled absorbers, including aperture efficiency, throughput, and beam patterns. Compared with bare absorbers, lens-coupled absorbers exhibit reduced sensitivity to noise from both the instrument enclosure and the sky background. We analyze FPA sampling strategies in terms of relative observing speed, considering both detector noise-limited and background noise-limited scenarios. In the background noise-limited case, near-maximum-gain sampling is optimal only when the point spread function (PSF) in the reflector focal plane is aligned with the lens. For arbitrary PSF incidence, a near-Nyquist sampling configuration provides the best average performance. These calculations are based on a computationally efficient quasi-analytical technique and assume a hex-packed array of circular lenses, recently developed for PRIMA.

> © The Authors. Published by SPIE under a Creative Commons Attribution 4.0 International License. Distribution or reproduction of this work in whole or in part requires full attribution of the original publication, including its DOI. [DOI: 10.1117/1.JATIS.11.3.031613]

> **Keywords:** kinetic inductance detectors; far-infrared; observing speed; signal-tonoise ratio; lens-coupled absorbers; spectroscopy; spectro-photometry; imaging; astrophysics; focal plane array; sampling

> Paper 25029SS received Feb. 3, 2025; revised Mar. 25, 2025; accepted Mar. 31, 2025; published May 5, 2025.

1 Introduction

The PRobe far-Infrared Mission for Astrophysics (PRIMA) is an actively cooled, space-borne far-infrared (FIR) observatory mission concept designed to study a broad range of astrophysical phenomena, including galaxy evolution and planetary system formation, using spectrophotometry techniques. ^{1,2} The observatory will feature a multiband imager (PRIMAger) and a long-slit grating spectrometer (FIRESS), covering several bands in the FIR range from 24 to 250 μ m.

PRIMA aims to bridge the observational gap between the ground-based atacama large millimeter/submillimeter array (ALMA) observatory and the space-borne James Webb Space Telescope (JWST), offering orders of magnitude better mapping speed than its FIR predecessors,

^{*}Address all correspondence to Sven van Berkel, sven.l.van.berkel@jpl.nasa.gov

such as Photodetector Array Camera and Spectrometer (PACS) and Spectral and Photometric Imaging Receiver (SPIRE) on Herschel.³ Both instruments will employ cryogenically cooled (<150 mK) lens-coupled kinetic inductance detectors (KIDs) as focal plane array (FPA) elements, operating at the fundamental sensitivity limit imposed by natural astrophysical backgrounds, such as solar system and galactic dust emission. The operating principle of KIDs relies on absorbed photons altering the inductance and, consequently, the resonant frequency of a superconducting resonator.⁴

Radiation can be coupled into KIDs via an antenna structure or a multi-mode absorber, the latter typically associated with lumped-element KIDs (LEKIDs). Practically, some form of areal concentration is required to construct the focal planes (FPs), and both feedhorns and lenses are commonly used as concentrators. PRIMA's detector development has primarily focused on LEKIDs with multi-mode patterned absorbers coupled to silicon lenses. ⁵⁻⁷ This approach provides design flexibility and is particularly suited for the short wavelengths (down to $24 \mu m$) required for PRIMA.

This paper investigates reflector FP sampling strategies for FPAs filled with lens-coupled absorbers, optimized for spectrophotometry. It is well known that FP sampling entails a trade-off among detector efficiency, angular resolution of on-sky beams, and sensitivity to the sky background. In astronomical photometry, power spread across multiple pixels can be summed to maximize the signal-to-noise ratio (SNR) and achieve the fastest possible observing speed. The effectiveness of this summation strongly depends on the FP sampling periodicity. An extensive study of relative observing speeds as a function of FPA sampling periodicity, comparing bare absorbers and feedhorn-coupled absorbers, was conducted in Ref. 9. A comparative study between bare absorbers and antennas is presented in Ref. 10, whereas wideband antenna FPAs are studied in Ref. 11. However, these existing studies do not fully address the performance of PRIMA's FPA architecture, as its focal plane elements differ fundamentally.

Lens-coupled absorbers share multi-mode characteristics with bare absorbers while also inheriting focusing properties from the lens, similar to antennas. Power incident on the lens is diffracted toward a small absorber (i.e., the KID inductor) located at the lens focal plane, introducing additional spillover losses. This effectively reduces the beam solid angle (i.e., enhances focusing) of the angular reception pattern of a quasi-optically coupled absorber compared with a bare absorber. ¹⁰ This unique combination of properties necessitates a dedicated study. In this work, we study sampling considerations for a hex-packed array of circular lenses recently developed for PRIMA in a 1008-pixel array format. ¹²

The paper is structured as follows. Section 2 defines the focal plane elements and details the quasi-analytical technique used to analyze coupling efficiency to a point source. Section 3 explores the fundamental characteristics of lens-coupled absorbers, including aperture efficiency, beam patterns, throughput, and resolution, and compares them to bare absorbers. Section 4 presents the methodology for analyzing observing speed as a function of FP sampling periodicity, comparing scenarios where a point source is aligned or misaligned with a pixel. Section 5 applies this methodology to PRIMA's spectrometry and two-dimensional (2D) imaging use cases to determine the optimal reflector FP sampling configuration. Section 6 discusses potential performance improvements using hexagonal micro-lenses with a 100% fill factor and investigates different absorber sizes. Section 7 summarizes the optimal reflector sampling configurations for PRIMA.

2 Focal Plane Array Definition and Quasi-Analytical Model

A generalized schematic representation of the optical geometry is shown in Fig. 1(a). The system consists of an on-axis parabolic reflector with a focal number of $f_{\#}^{\rm refl} = F^{\rm refl}/D^{\rm refl}$ and a hexagonal FPA with sampling periodicity d_f . Each FPA element is a lens-coupled absorber, as illustrated in Fig. 1(b). The lens, with refractive index $n^{\rm lens}$, has a clear aperture diameter d_l and a nominal focal number $f_{\#}^{\rm lens} = F^{\rm lens}/d_f$. The lens is equipped with an anti-reflection (AR) coating of refractive index $n^{\rm AR}$ and thickness $t^{\rm AR}$. An absorber with dimension $w_{\rm abs}$ is placed in the lens FP. Ideally, the absorber should be backed by a reflective layer at a quarter-wavelength distance to maximize optical efficiency, though this introduces added fabrication complexity.

The optimal lens focal number and absorber size depend on several parameters, including stratification, wavelength, micro-lens fabrication constraints, angular absorber response, and

Fig. 1 FPA configuration. (a) Simplified optics and lens-coupled FPA. (b) Schematic representation of typical lens-coupled absorbers with key geometrical parameters. (c) Generalized electromagnetic model illustrating an ideal absorber capturing the direct field in the lens FP. (d) Power geometrically available to a virtual, perfect absorber in the lens FP.

KID responsivity (which itself depends on absorber volume). Typically, the relative absorber size is targeted to be $w_{\rm abs} \approx 2 f_{\#}^{\rm lens} \lambda_d$, where λ_d is the wavelength in the lens medium, to maximize optical efficiency while minimizing absorber volume. To maintain generality in our results, we do not specify a particular stratification or absorber design. Instead, we introduce the generalized electromagnetic model depicted in Fig. 1(c), which consists of a lens with an infinitely extended half-space below the absorber plane (i.e., the lens FP). We consider a virtual absorber placed in this plane that absorbs all geometrically available power, as illustrated in Fig. 1(d). Similar to the analysis in Ref. 9, this work presents a study of relative observing speed as a function of FP sampling. Using a relative comparison, the effects of parameters independent of FP sampling (e.g., absorptance and angular absorber response) largely cancel out. Consequently, the recommendations derived from this study are applicable not only to PRIMA but also to a broad range of lens and absorber configurations.

Details regarding the specific micro-lens geometry used in the relative observing speed analysis are provided in Appendix A. This study assumes the baseline lens-coupled absorber geometry developed for PRIMA's longest wavelength band in the FIRESS spectrometer. The analysis employs 1008-pixel micro-lens arrays fabricated using greyscale lithography at the National Aeronautics and Space Administration's (NASA's) Goddard Space Flight Center (GSFC). A clear aperture diameter of approximately $d_l = 0.93d_f$ is used, as this represents the current state-of-the-art. However, in Sec. 6, we compare these results with those obtained using an array of ideal hexagonal lenses with a 100% fill factor, as continued advancements in greyscale etching technology are anticipated.

PRIMA is designed with four spectral bands, each with a 1:1.8 relative bandwidth. We investigate observing speed at the geometric mean wavelength (λ_{c0}) and at the band edge wavelengths (0.75 λ_{c0} and 1.35 λ_{c0}). The power geometrically available to the absorber is computed using an efficient Fourier optics (FO) based model, based on the theoretical work established in Refs. 10, 13, and 14. A full description of the quasi-analytical model, along with validation using full-wave simulations for the reference case of the relative observing speed study, is provided in Appendix B.

3 Fundamental Characteristics of Lens-Coupled Absorbers

Lens-coupled absorbers inherit the multi-mode properties of bare absorbers and can couple to more than a single mode's throughput. At the same time, the coherent properties of the dielectric focusing lens placed above the absorber modify the angular response of the FP element, deviating from Lambert's cosine law and affecting resolution and throughput. In this section, we present the fundamental characteristics of FPAs filled with lens-coupled absorbers, including efficiency, element beam patterns, normalized throughput from the sky background, instrument on-sky beam patterns, and imaging resolution.

3.1 Aperture Efficiency

The reflector aperture efficiency when using lens-coupled absorbers is determined by several factors: the fraction of the point spread function (PSF) power in the reflector FP that spills beyond

the clear lens aperture, reflections at the dielectric interface, dielectric losses in the lens medium, the fraction of the PSF power in the lens FP that spills beyond the absorber, and the absorptance of the absorber. Dielectric losses in HRFZ-Si are negligible for wavelengths $\lambda_0 > 20~\mu m$, particularly at cryogenic temperatures, but may be significant at shorter wavelengths. ¹⁵ In this study, we assume lossless lenses and perfect absorptance to keep the analysis independent of the specific absorber implementation. The aperture efficiency is defined as

$$\eta_{\rm ap} = \eta_{\rm so} \eta_{\rm lens},\tag{1}$$

where η_{so} represents the spillover efficiency in the reflector FP, and η_{lens} accounts for lenslet efficiency, including reflection and spillover losses in the absorber plane. By definition, these efficiencies are calculated for a single pixel with an aligned point source in the far field of the reflector (i.e., plane wave incidence). The aperture efficiency is assumed to be uniform across all pixels in the array.

The spillover losses in the reflector FP for different FPA packing architectures as a function of reflector FP sampling d_f are shown in Fig. 2(a). In this study, the physical FP sampling remains fixed, whereas the reflector focal number varies. A square-packed array with a 100% fill factor has a unit cell area $1.155 \times$ larger than that of a hex-packed array with 100% fill-factor hexagonal lenses, resulting in higher spillover efficiency, especially for tight FPA sampling. A circular lens with diameter $d_l = d_f$ in a hex-packed array has a 90.7% fill factor. The micro-lens arrays baselined for PRIMA's FIRESS long-wavelength band, discussed in Appendix A, have a clear diameter of approximately $d_l = 0.93d_f$, corresponding to a 78.4% fill factor.

The spillover losses in the lens FP for square and circular absorbers as a function of absorber side length or diameter w_{abs} are shown in Fig. 2(b). The calculations assume a reflector FP sampling of $d_f = 1f_{\#}^{refl}\lambda_0$, meaning the lens is relatively uniformly illuminated. Square absorbers

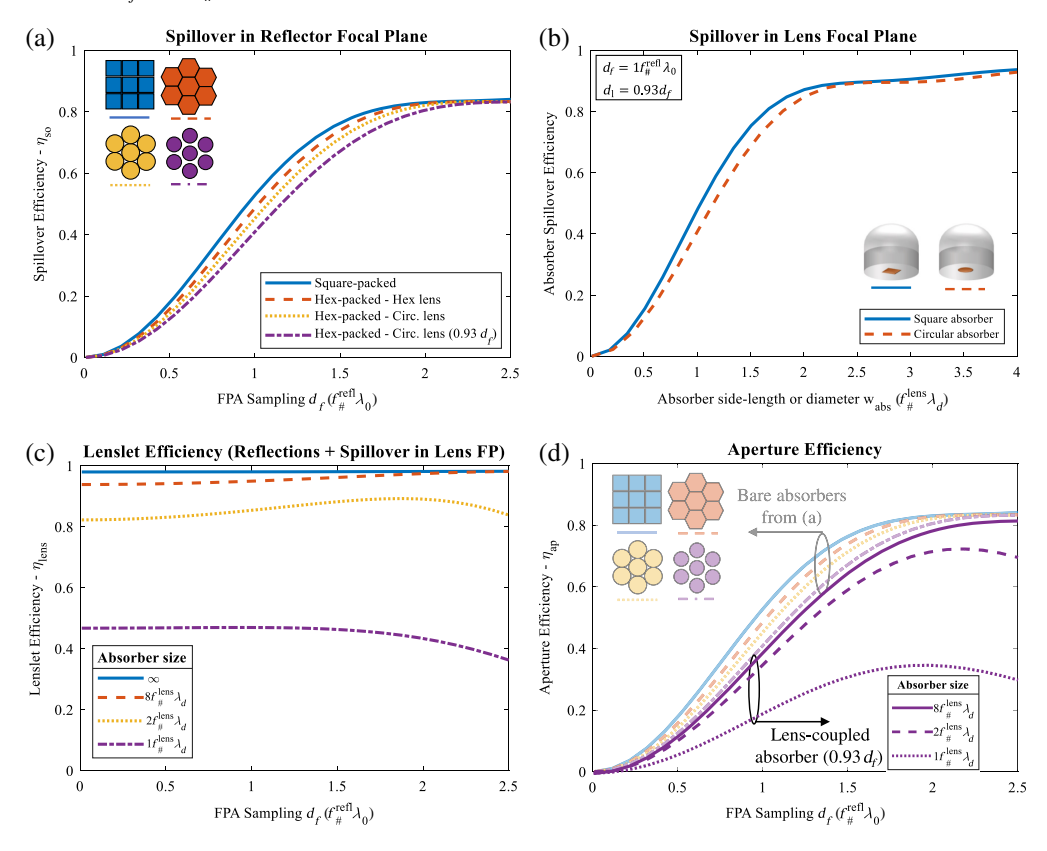


Fig. 2 Comparison of aperture efficiency for bare absorbers and lens-coupled absorbers. (a) Spillover efficiency in the reflector FP for different FPA packing architectures. (b) Spillover efficiency in the lens FP for square or circular absorbers. (c) Lenslet efficiency for different absorber sizes w_{abs} . (d) Aperture efficiency of lens-coupled absorbers for different absorber sizes w_{abs} compared with bare absorbers (transparent overlay).

have a 27% larger area and therefore show higher efficiency. However, a circular absorber is generally better matched to the circular PSF for an aligned point source, making it more efficient for the same absorber volume. An absorber size of $w_{\rm abs} = 2f_{\#}^{\rm lens} \lambda_d$ should be targeted to achieve ~85% spillover efficiency, where $\lambda_d = \lambda_0/n^{\rm lens}$ is the wavelength in the dielectric.

The lenslet efficiency as a function of reflector FP sampling d_f for different square absorber sizes $w_{\rm abs}$ is shown in Fig. 2(c). An absorber size of $w_{\rm abs} = \infty$ represents the case where only reflection losses at the lens surface are considered. These contribute to a ~2% reduction in lenslet efficiency when the AR-coating thickness is exactly a quarter-wavelength (see Appendix A and B for details on the AR coating). For large but finite absorbers $(w_{\rm abs} > 2f_{\#}^{\rm lens}\lambda_d)$, a slight increase in lenslet efficiency is observed for increasing FPA sampling periodicity due to reduced sidelobe power spilling outside the absorber region. For very sparse FPA sampling $(d_f > 2f_{\#}^{\rm refl}\lambda_0)$, the lens becomes significantly under-illuminated, increasing spillover losses for small absorbers $(w_{\rm abs} < 2f_{\#}^{\rm lens}\lambda_d)$ as the main lobe grows larger than the absorber.

The aperture efficiency from Eq. (1) of lens-coupled absorbers as a function of FP sampling d_f for different absorber sizes $w_{\rm abs}$ is shown in Fig. 2(d). Included in the figure as a transparent overlay is the aperture efficiency of bare absorbers, which corresponds to the spillover efficiency from Fig. 2(a). Overall, lens-coupled absorbers generally have a lower aperture efficiency, primarily due to the reduced fill factor of the FPA, spillover on the finite-sized absorber, and to a lesser extent, reflections at the lens surface.

3.2 Focal Plane Element Angular Response Patterns and Background Throughput

The angular response patterns for the FP elements are shown in Fig. 3(a), with bare absorbers on the left-hand side and lens-coupled absorbers on the right-hand side. The angular response pattern of a bare absorber follows Lambert's cosine law and remains independent of its physical size, w_{abs} , and shape due to its inherently multi-mode nature. This is not the case for lens-coupled absorbers, where the angular response depends on absorber shape and size, lens geometry, and polarization.

The angular response patterns for the microlenses described in Appendix A are analyzed for three different square absorber sizes. The shaded regions in Fig. 3(a) represent the upper and lower boundaries of the response patterns in the principal planes. These pattern cuts are not identical due to the differing Fresnel reflection and transmission coefficients for perpendicular and parallel polarization. Dashed vertical lines indicate reflector truncation angles corresponding to different FP sampling configurations.

Lens-coupled absorbers are potentially less susceptible to stray light from the instrument enclosure. However, the absorber still exhibits a cosine-shaped angular response pattern within the lens material, making it vulnerable to cross-coupling inside the lens array. This cross-coupling could be partially mitigated by incorporating an absorbing titanium mesh grid between the lens and detector wafer, as demonstrated in Ref. 16.

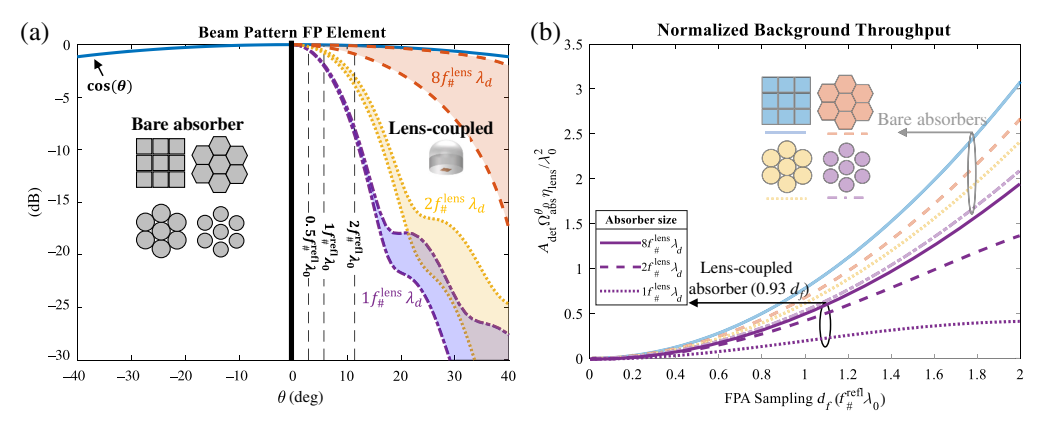


Fig. 3 Comparison of angular power reception pattern and background throughput for bare absorbers and lens-coupled absorbers. (a) The angular response pattern of bare absorbers (left) and lens-coupled absorbers as a function of absorber size (right). (b) Normalized throughput (with a transparent overlay for bare absorbers).

Unlike bare absorbers, lens-coupled absorbers do not view the telescope with a top-hat beam and $\pi/(2f_{\#}^{\rm refl})^2$ beam solid-angle. As a result, their throughput for external background radiation is lower. The normalized throughput is calculated as $\frac{A_{\rm det}\Omega_{\rm abs}^{\theta_0}\eta_{\rm lens}}{\lambda_0^2}$, where $A_{\rm det}$ is the area of the lens clear aperture or bare absorber, and $\Omega_{\rm abs}^{\theta_0}$ represents the beam solid angle of the reflector as seen by the beam pattern of the (lens-coupled) absorber. The results are shown in Fig. 3(b).

Lens-coupled absorbers exhibit lower throughput due to a smaller beam solid angle, though this comes at the cost of increased spillover losses in the lens FP. Consequently, lens-coupled absorbers are less sensitive to sky background noise and provide improved imaging resolution, characterized by narrower on-sky beams compared with bare absorbers.

3.3 On-Sky Beams and Imaging Resolution

The aperture efficiency, $\eta_{\rm ap}$ (1), quantifies the coupling efficiency of a lens-coupled absorber to a point source in the far field of the reflector, assuming that the PSF in the reflector FP is centered on the FP element. The normalized on-sky beam pattern, F_i , is defined as the variation in coupling efficiency for different point source locations, where the PSF in the reflector FP is misaligned with the FP element. Mathematically, the coupling efficiency for feed i to a point source located at spherical coordinates (θ_s, ϕ_s) is given by

$$\eta_{\text{co},i}(\lambda_0, \theta_s, \phi_s) = \eta_{\text{ap}}(\lambda_0) F_i(\lambda_0, \theta_s, \phi_s). \tag{2}$$

The on-sky beam patterns for the centered FP element (i = 1) are evaluated in one principal plane (TM-polarized) and presented in Fig. 4(a). The left-hand side shows the results for square bare absorbers, whereas the right-hand side depicts the results for the lens-coupled absorber. Four different reflector FP sampling periodicities are analyzed, and full-wave validation points, shown as crosses, demonstrate excellent agreement with the model. For very small sampling periodicity, the on-sky beam pattern converges to the well-known airy disc and progressively widens with increasing periodicity. The deep nulls observed in coherent detection disappear due to incoherent detection effects. The on-sky beam patterns for bare absorbers are significantly wider than those of lens-coupled absorbers, contributing to the higher background throughput shown in Fig. 3(b).

The imaging resolution, defined here as the full width at half maximum of the on-sky pattern, is plotted in Fig. 4(b) as a function of reflector FP sampling periodicity for both bare absorbers (shown with a transparent overlay) and lens-coupled absorbers with different square absorber sizes. The square bare absorbers achieve the highest aperture efficiency [see Fig. 2(d)] due to their large collection area, though this comes at the expense of reduced resolution. The upper and lower bounds of the blue-shaded region in Fig. 4(b) indicate the resolution in the diagonal and

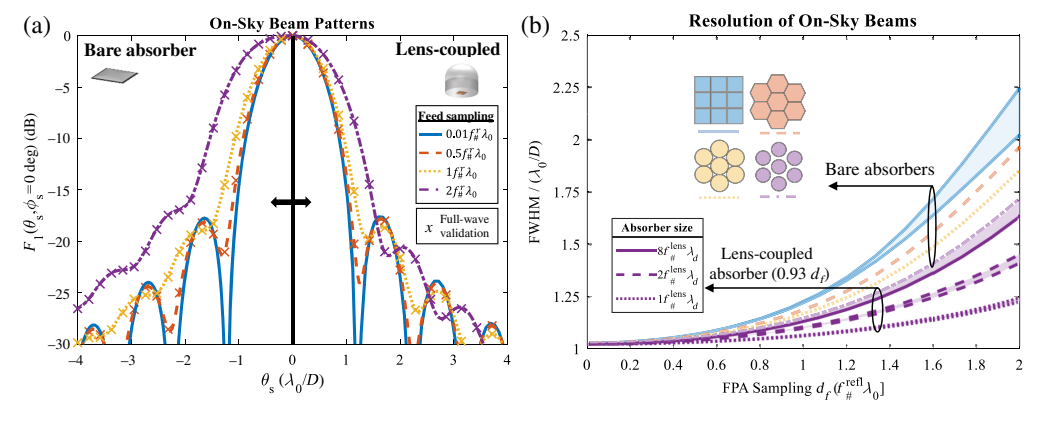


Fig. 4 (a) On-sky beam pattern cut (TM-polarized) for different reflector FP sampling periodicities. Left: bare absorber-filled FPAs (square). Right: lens-coupled absorber-filled FPAs from Appendix A with $w_{\rm abs} = 2f_{\#}^{\rm lens} \lambda_d$. Full-wave simulation validation points are indicated by crosses. (b) Resolution of different bare absorber FPA architectures and lens-coupled absorbers with varying square absorber sizes.

main planes, respectively. The beams of hexagonal and circular bare absorbers are symmetric. However, the on-sky beam patterns of lens-coupled absorbers can be asymmetric due to the same effects discussed in the previous section. A near-diffraction-limited resolution can be achieved using lens-coupled absorbers with small absorber sizes, albeit at the cost of reduced aperture efficiency.

4 Observing Speed for Aligned and Misaligned Point-Source Extraction

The previous section demonstrated that the FPA sampling periodicity not only influences aperture efficiency but also determines imaging resolution and the throughput of sky background noise. Consequently, careful FPA sampling considerations are required to maximize the SNR and observing speed. This section presents an analysis of relative observing speed for (spectro-)photometry, considering both single-pixel and multi-pixel photon flux estimation methods, in the case that the source is aligned with the pixel. In addition, we examine the potential degradation in observing speed in scenarios where the point source location is misaligned.

A useful methodology to explore different FPA sampling configurations without requiring explicit definitions of FP sampling-independent quantities—such as the spectral brightness of the sky background, telescope emission, or pixel bandwidth—was proposed by Griffin et al. In this approach, the SNR of a pixel within a given architecture is evaluated relative to the SNR of a fixed reference case for a given integration time.

We define the reference case as a lens-coupled absorber with a sampling periodicity of $d_f = 2f_\#^{\rm refl}\lambda_{0c}$ and a square absorber of size $w_{\rm abs} = 2f_\#^{\rm lens}\lambda_{dc}$. The PSF is assumed to be perfectly aligned with the pixel, as illustrated in Fig. 5(a). The aperture efficiency, $\eta_{\rm ap,ref}$, and normalized angular response pattern, $F_{1,\rm ref}$, for this reference geometry—along with validation using full-wave simulations—are presented in Appendix Figs. 11(a) and 11(b), respectively.

4.1 Relative Observing Speed for an Aligned Point Source Using a Single Pixel We first analyze the relative observing speed in the case where a single pixel observes an aligned point source. Using the SNR expression from (22), derived in Appendix C, the ratio of the SNR

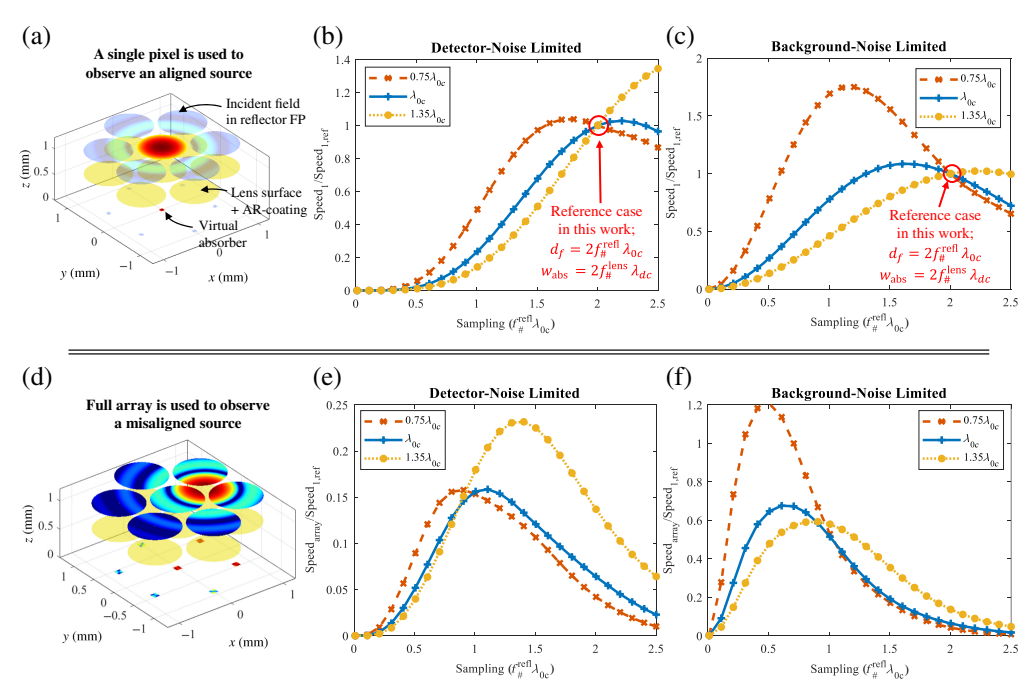


Fig. 5 Relative observing speed for various observing scenarios. (a)–(c) Single pixel observes an aligned point source. (d)–(f) Full array observes a misaligned point source where the PSF impinges at the corner of three pixels.

for pixel i in the considered architecture, SNR_i , to the SNR of the reference case, $SNR_{1,ref}$, is given by

$$\frac{\text{SNR}_i}{\text{SNR}_{1,\text{ref}}} = \frac{\eta_{\text{co},i}}{\eta_{\text{ap,ref}}} \frac{\text{NEP}_{\text{ref}}}{\text{NEP}},$$
(3)

where noise equivalent power (NEP) represents the noise equivalent power, which includes both detector noise and photon noise. The NEP is assumed to be the same for every pixel, as we consider faint sources. As the SNR scales with the square root of integration time, the relative observing speed is proportional to the square of the relative SNR. The optimal FPA sampling configuration depends on whether the NEP (15) is dominated by detector noise or background noise. We analyze these two limiting cases separately, assuming an aligned PSF at the center FP element (i = 1)

$$\frac{|Speed_1|}{|Speed_1|_{ref}} \Big|_{NEP_{det} \gg NEP_{ph}} = \left(\frac{\eta_{ap}}{\eta_{ap,ref}}\right)^2, \tag{4a}$$

$$\frac{\text{Speed}_{1}}{\text{Speed}_{1,\text{ref}}}\bigg|_{\text{NEP}_{\text{det}} \ll \text{NEP}_{\text{ph}}} = \left(\frac{\eta_{\text{ap}}}{\eta_{\text{ap},\text{ref}}}\right)^{2} \frac{\eta_{\text{ap,ref}} \Omega_{\text{instr},\text{ref}}}{\eta_{\text{ap}} \Omega_{\text{instr}}} = \frac{\eta_{\text{ap}} \Omega_{\text{instr},\text{ref}}}{\eta_{\text{ap},\text{ref}} \Omega_{\text{instr}}},$$
(4b)

where $\Omega_{\text{instr}} = \int_{2\pi} \int_{\pi/2} F_1(\theta, \phi) \sin(\theta) d\theta d\phi$ is the beam solid angle of the on-sky beam patterns, which is assumed to be uniform across all pixels. Unlike the mapping speed analyses in Refs. 9 and 11, we do not account for additional time penalties associated with telescope jiggling to achieve full spatial sky sampling. PRIMA will perform 2D mapping using a combination of a steering mirror and an observatory scan, as described later in Sec. 5.

For the detector noise-limited case, detector noise cancels out, and the relative observing speed is proportional to the squared ratio of the aperture efficiencies. In the background noise-limited case, the relative observing speed increases linearly with aperture efficiency, as NEP scales with the square root of efficiency. As expected, observing speed decreases with increasing instrument solid angle due to greater sky background power integration.

The aperture efficiency is plotted as the blue curve in Fig. 6(a) as a function of sampling periodicity. In addition, the purple dash-dotted line represents a figure of merit indicating how focused the on-sky beam pattern is relative to the diffraction-limited case, given by $\Omega_{\rm Airy}/\Omega_{\rm instr}$. The beam solid angle of the diffraction-limited airy disc depends on the wavelength and the reflector area and is defined as $\Omega_{\rm Airy}=\lambda_0^2/A_{\rm refl}$. We refer to this figure of merit as focusing efficiency.¹⁰

The relative observing speed for both limits in Eq. (4) is presented in Figs. 5(b) and 5(c) for the sampling wavelength λ_{c0} , as well as the band edges of FIRESS at $0.75\lambda_{c0}$ and $1.35\lambda_{c0}$. In a detector noise–imited scenario, sparse sampling is preferred across the entire band, as it

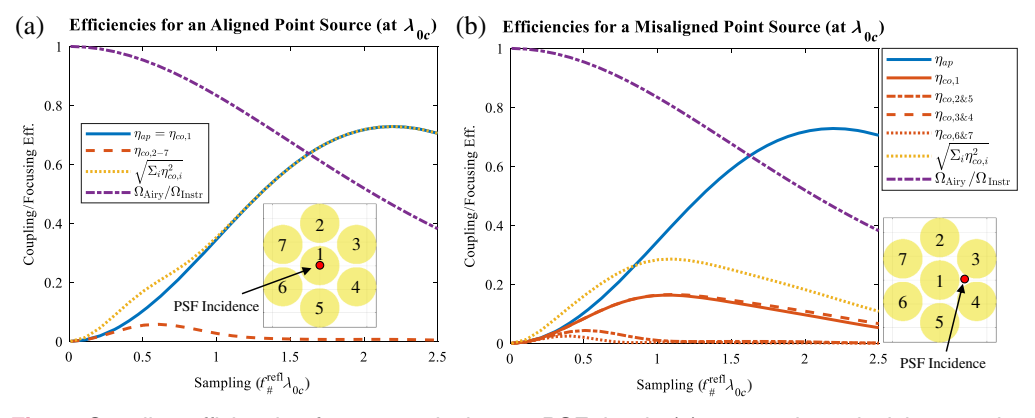


Fig. 6 Coupling efficiencies for seven pixels to a PSF that is (a) centered on pixel i=1 and a (b) PSF centered at the corner among pixels i=1,3, and 4. The quadrature sum (yellow dotted), aperture efficiency (blue solid), and focusing efficiency of the on-sky beam pattern $\Omega_{\text{Airy}}/\Omega_{\text{Instr}}$ (dash-dotted purple) are also shown.

maximizes aperture efficiency. In a background noise-limited scenario, the optimal sampling occurs at the crossover point of aperture efficiency and focusing efficiency [dash-dotted purple curve in Fig. 6(a)], corresponding to $d_f = 1.6 f_\#^{\text{refl}} \lambda_{0c}$. At this sampling periodicity, the relative observing speed reaches 1.08, compared with 0.27 for a fully sampled array and 0.77 for a $d_f = 1.0 f_\#^{\text{refl}} \lambda_{0c}$ sampled array.

For sparsely sampled arrays, significant degradation in observing speed is expected at the shortest wavelength of the band, as evident from the $0.75\lambda_{c0}$ curve. This degradation results from increased background throughput and reduced aperture efficiency due to under-illumination of the lens by the PSF.

4.2 Relative Observing Speed Using Multiple Pixels

Tightly sampled FPAs inherently distribute the power of a PSF across multiple pixels. By co-adding signals (and noise) from neighboring elements, the SNR can be improved. ^{8,9} In this summation, we consider a hexagonal array of seven elements that can potentially receive a non-negligible amount of power from the point source. As shown in Appendix D, the SNR when using multiple pixels can be expressed as a quadrature sum of the individual pixel SNRs.

4.2.1 Aligned point source

We first consider the case where the PSF is aligned with a central pixel, but all pixels in the array contribute to estimating the flux. The observing speed, when using the full array, increases by a factor of

$$N_{\text{array}} = \left(\frac{\sqrt{\sum_{i} \eta_{\text{co},i}^2}}{\eta_{\text{ap}}}\right)^2.$$
 (5)

The coupling efficiency for the central pixel, $\eta_{co,1} = \eta_{ap}$, the surrounding pixels, $\eta_{co,2-7}$, and their quadrature sum (termed as array efficiency), are shown in Fig. 6(a). It can be observed that summing power from multiple pixels is beneficial only for tight sampling configurations where $d_f < 1f_\#^{\rm refl}\lambda_{0c}$. For a fully sampled array with $d_f = 0.5f_\#^{\rm refl}\lambda_{0c}$, the observing speed improvement when using the full array is $N_{\rm array} = 2.71$. However, this improvement decreases rapidly with increasing sampling periodicity, dropping to $N_{\rm array} = 1.01$ for $d_f = 1f_\#^{\rm refl}\lambda_{0c}$. The relative observing speed as a function of FP sampling, still referenced to the same baseline case where only the center pixel is used, is shown later in Figs. 8(a)–8(c). The optimal sampling configuration remains unchanged at $d_f = 1.6f_\#^{\rm refl}\lambda_{0c}$.

4.2.2 Misaligned point source

The previous analysis assumed that the PSF was aligned with the center pixel of the seven-pixel hexagonal grid. However, sensitivity varies significantly depending on the source position, referred to as pixel phase, particularly for sparse sampling. The worst-case scenario occurs when the PSF is centered at the corner of a hexagonal unit cell, as illustrated in Fig. 5(d).

The coupling efficiencies for each pixel, and their quadrature sum, in this scenario are shown in Fig. 6(b). For a fully sampled array, the coupling efficiency $\eta_{\text{co},1}$ is only slightly lower than the aperture efficiency, as the PSF is significantly larger than the lens diameter and efficiently illuminates three pixels. This slight reduction is fully compensated by summing the power from pixels 3 and 4, resulting in an array efficiency exceeding the aperture efficiency for sampling periodicities of $d_f < 0.85 f_{\#}^{\text{refl}} \lambda_{0c}$. For $d_f > 0.85 f_{\#}^{\text{refl}} \lambda_{0c}$, the quadrature sum of coupling efficiencies remains effective but becomes significantly smaller than the aperture efficiencies due to two main factors. First, the lens becomes highly under-illuminated, increasing spillover losses at the absorber as the PSF in the lens FP expands (see Fig. 10 for an example of a misaligned PSF). Second, a significant fraction of the PSF does not overlap with clear lens apertures, as the fill factor of the hexagonal grid is below 100%.

The resulting relative observing speed is shown in Figs. 5(e) and 5(f), where it is evident that the optimal sampling periodicity is significantly smaller. For detector noise–limited systems, observing speed is maximized at $d_f = 1.1 f_\#^{\text{refl}} \lambda_{0c}$ but remains 0.16× lower than the aligned case. In background noise–limited systems, optimal sampling occurs at $d_f = 0.7 f_\#^{\text{refl}} \lambda_{0c}$, with an observing speed 0.60× lower than the aligned case.

Different sampling configurations may be optimal depending on the measurement type and possible pixel phases. In the next section, we investigate different scenarios relevant to PRIMA.

5 PRIMA Case Study: Average Observing Speed for FIR Spectrometry and Imaging

We now apply this formalism to evaluate the effective, average observing speed as a function of detector sampling for various PRIMA measurement scenarios. We consider three distinct cases, each associated with relevant pixel phases, as indicated by letters a to e in Fig. 8. The three scenarios are as follows:

- a. Pointed: The aligned/pointed case from Sec. 4.2, which serves as a limiting case. This approximately applies to point-source spectroscopy with FIRESS when targeting a spectral line with a known frequency. PRIMA's pointing precision is sufficient to center a source within a pixel, and the staggered spectral rows ensure that any given frequency can be nearly centered on a pixel. FIRESS will use the steering mirror to chop the source along the slit to provide modulation.
- b. **Spectrometer**: A more general FIRESS scenario in which we average over the spectral row at a given spatial position. FIRESS will chop among staggered spectral rows to provide uniform spectral coverage, and the equivalent sensitivity is obtained by averaging over the pixel phases shown in Fig. 8(d).
- c. **Imager**: A full 2D imaging scenario, relevant from PRIMAger, in which the effective sensitivity is determined by averaging over all pixel phases shown in Fig. 8(g).

5.1 Average Array Efficiency

For each scenario, the SNR is averaged over the relevant pixel phases using appropriate weights. The SNR of the array for a given pixel phase $\phi = a \rightarrow e$, denoted as SNR_{array}^{ϕ} , is expressed as

$$SNR_{array}^{\phi} = \frac{\eta_{array}^{\phi} P^{PSF}}{NEP} \sqrt{2\tau_{int}},$$
 (6a)

$$\eta_{\text{array}}^{\phi} = \sqrt{\sum_{i} \eta_{\text{co},i}^{2}(\theta_{s}^{\phi}, \phi_{s}^{\phi})},$$
(6b)

where P^{PSF} represents the total power in the reflector FP, and $\eta_{\text{array}}^{\phi}$ is the quadrature-summed array efficiency for pixel phase ϕ (i.e., for a point source located at θ_s^{ϕ} , ϕ_s^{ϕ}). The average SNR, $\overline{\text{SNR}}_{\text{array}}$, given by (7a), depends on the averaged array coupling efficiency, $\overline{\eta}_{\text{array}}$. The overline denotes an averaged quantity, calculated using Eq. (7b) for each of the three considered scenarios. The averaging accounts for the fact that pixel phases at hexagonal corners and edges are shared among adjacent pixels

$$\overline{\text{SNR}}_{\text{array}} = \frac{\overline{\eta}_{\text{array}} P^{\text{PSF}}}{\text{NEP}} \sqrt{2\tau_{\text{int}}}, \tag{7a}$$

$$\overline{\eta}_{\text{array}} = \begin{cases}
\eta_{\text{array}}^{a} & \text{Pointed} \\
\frac{\eta_{\text{array}}^{a} + \eta_{\text{array}}^{d} + 2\eta_{\text{array}}^{e}}{4} & \text{Spectrometer} \\
\frac{\eta_{\text{array}}^{a} + 6\eta_{\text{array}}^{b} + 2\eta_{\text{array}}^{c} + 3\eta_{\text{array}}^{d}}{12} & \text{Imager}
\end{cases}$$
(7b)

The resulting average array efficiencies at the central and boundary wavelengths are shown in Fig. 7. As discussed in Sec. 4.2, the array efficiency for an aligned PSF (solid blue) at λ_{0c} exceeds the aperture efficiency for tight sampling configurations up to $d_f = 0.85 f_\#^{\text{refl}} \lambda_{0c}$, after which it

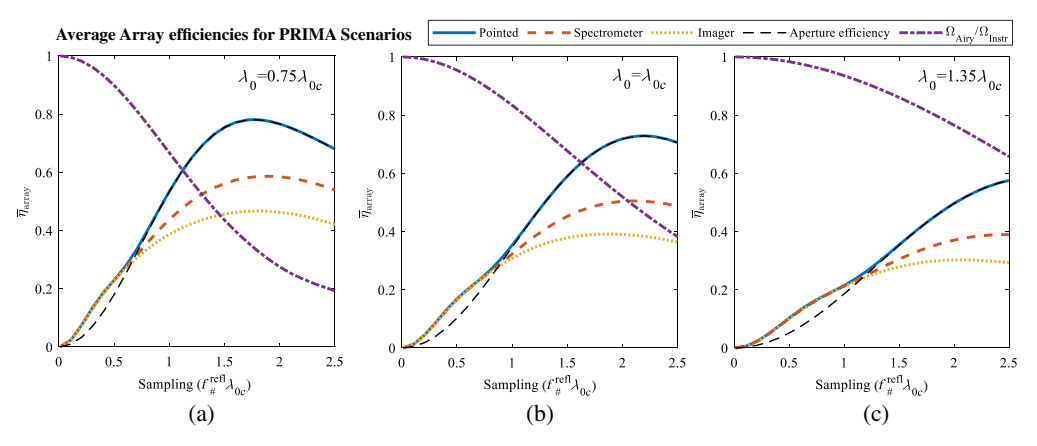


Fig. 7 Average array efficiency and focusing efficiency (dash-dotted purple) at $\lambda_0 = 0.75\lambda_{0c}$ (a), λ_{0c} (b), and $1.35\lambda_{0c}$ (c), as defined in Eq. (7b). The aligned PSF case (solid blue), spectrometer scenario (dashed red), and imager scenario (dotted yellow) are shown. For reference, the aperture efficiency (dashed black) is also plotted.

converges to the aperture efficiency (dashed black). The average array efficiency for the spectrometer (dashed red) and imager (dotted yellow) follows a similar trend for tight sampling but reaches a maximum efficiency of 50% and 39%, respectively, compared with 73% for the aligned PSF case.

When efficiencies are compared across different wavelengths, it is evident that the optimal reflector FP sampling periodicity scales linearly with wavelength. However, the absolute efficiency values decrease due to absorber spillover losses, as the absorber size remains constant.

5.2 Average Observing Speed

The relative SNR of the array, averaged over different pixel phases and still compared with the aligned reference case using a single pixel, is given by

$$\frac{\overline{SNR}_{array}}{SNR_{1,ref}} = \frac{\overline{\eta}_{array}}{\eta_{ap,ref}} \frac{NEP_{ref}}{NEP}.$$
(8)

The average relative observing speed, $\overline{\text{Speed}}_{\text{array}}/\text{Speed}_{1,\text{ref}}$, is obtained by squaring the average relative SNR in Eq. (8) and is summarized in Fig. 8 for all scenarios.

For a detector noise–limited system, a maximum gain sampled FP is optimal across all scenarios. Compared with the case of an aligned point source, the observing speed at the sampling wavelength λ_{0c} is reduced by a factor of 0.5 for the spectrometer scenario and by 0.3 for the imaging scenario. The observing speed at the edges of the frequency band, i.e., at $0.75\lambda_{0c}$ and $1.35\lambda_{0c}$, is also maximized for a maximum gain sampled array.

For a background noise–limited system, the optimal sampling configuration when the PSF is aligned corresponds to a moderately sparse sampling of $d_f = 1.6 f_{\#}^{\rm refl} \lambda_{0c}$, yielding a relative observing speed of 1.08. In the spectrometer scenario, the observing speed at λ_{0c} remains relatively constant as a function of reflector FP sampling, with an optimum value of 0.68 at $d_f = 0.6 f_{\#}^{\rm refl} \lambda_{0c}$. This stability occurs because the increasing aperture efficiency is counterbalanced by a decreasing coupling efficiency for misaligned point sources and an increasing throughput of sky background noise. At the shortest wavelength of the band, $0.75\lambda_{0c}$, the observing speed begins to decline rapidly for $d_f > 1.0 f_{\#}^{\rm refl} \lambda_{0c}$ due to a drop in aperture efficiency caused by significant under-illumination of the lens. The observing speed for the PRIMAger scenario is also maximized for a tight sampling configuration of $d_f = 0.6 f_{\#}^{\rm refl} \lambda_{0c}$, where the system achieves a relative observing speed of 0.65 at the sampling wavelength. Unlike the spectrometer scenario, the imaging speed does not remain constant as a function of sampling periodicity because the reduced off-axis performance contributes more significantly to the averaged array coupling efficiency Eq. (7b).

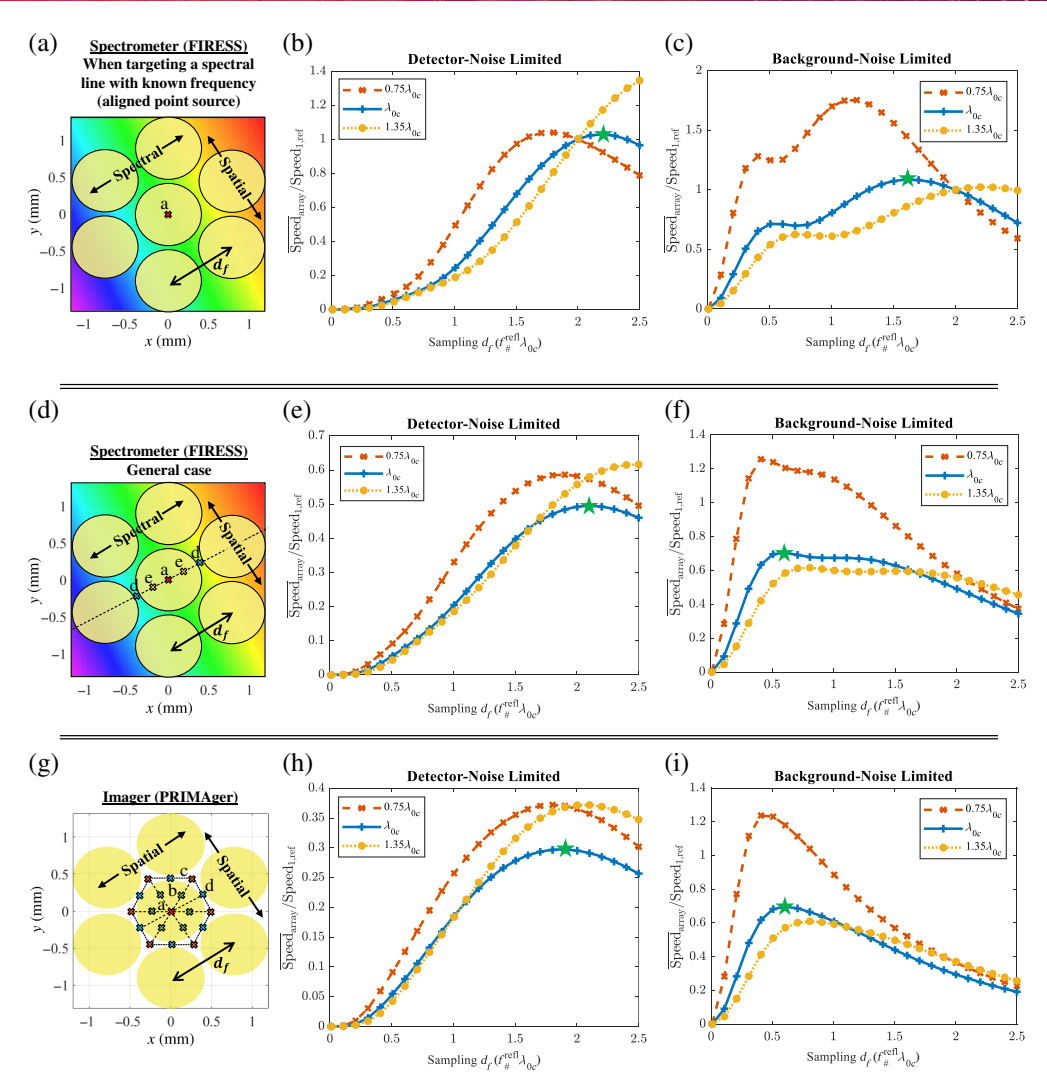


Fig. 8 Average relative observing speed for (a)–(c) the spectrometer scenario (FIRESS) targeting a spectral line with a known frequency, (d)–(f) the general spectrometer scenario (FIRESS), and (g)–(i) the 2D imaging scenario (PRIMAger). The left column illustrates the locations of PSF incidence in the reflector FP (i.e., pixel phases) used in the averaging process Eq. (7b). Results are shown for detector noise– and background noise–limited systems at the sampling wavelength and band edges.

The optimal sampling configurations are marked by a green star in Fig. 8, with their key system properties summarized in Table 1.

6 Perfect Hexagonal Microlenses and Different Absorber Sizes

Given the anticipated advancements in micro-lens array fabrication, it is valuable to investigate the performance of an FPA with a perfect hexagonal lens array featuring a 100% fill factor. In addition, we examine the effect of absorber size in greater detail to assess its impact on system performance.

6.1 Effect of Microlens Array Fill Factor

The aperture and focusing efficiencies for a hexagonal lens array with a 100% fill factor are represented by the hexagram-marked bound of the shaded regions in Fig. 9(a). For comparison, the circle-marked bound corresponds to the results from Fig. 7(b). In tightly sampled arrays $(d_f < 1f_\#^{\text{refl}}\lambda_{0c})$, where the lenses are illuminated quasi-uniformly, the aperture efficiency increases by a factor of $\sim 1.27 \times$, corresponding to the improvement in the fill factor. For larger

Table 1 Summary of optimal reflector sampling configurations.

	Pointed	Spectrometer	Imager
Detector noise limited			
Optimal sampling factor	$2.2f_{\#}^{\mathrm{refl}}\lambda_{0c}$	$2.1f_{\#}^{\mathrm{refl}}\lambda_{0c}$	$1.9f_{\#}^{\mathrm{refl}}\lambda_{0c}$
Relative observing speed ^a	1.03	0.49	0.30
(Average) array efficiency	73%	51%	39%
Aperture efficiency	73%	73%	70%
Angular resolution	$1.57\lambda_0/D$	$1.51\lambda_0/D$	$1.40\lambda_0/D$
Potential Rel. speed gain with increased fill factor ^b	1.07	1.39	1.64
Potential Rel. speed gain with increased absorber sizeb	1.24	1.54	1.69
Background noise limited			
Optimal sampling factor	$1.6f_{\#}^{ m refl}\lambda_{0c}$	$0.6f_{\#}^{\mathrm{refl}}\lambda_{0c}$	$0.6f_{\#}^{\mathrm{refl}}\lambda_{0c}$
Relative observing speed ^a	1.08	0.68	0.65
(Average) array efficiency	63%	20%	20%
Aperture efficiency	63%	15%	15%
Angular resolution	$1.27\lambda_0/D$	$1.05\lambda_0/D$	1.05λ ₀ / <i>D</i>
Potential Rel. speed gain with increased fill factor ^b	None	1.25	1.24
Potential Rel. speed gain with increased absorber size ^b	None	1.15	1.11

^aRelative to the speed of a $2f_{\#}^{\text{refl}}\lambda_{0c}$ lens with $2f_{\#}^{\text{lens}}\lambda_{dc}$ absorber, observing an aligned source (pointed).

sampling periodicities, this enhancement diminishes as the lenses become increasingly underilluminated. The maximum achievable aperture efficiency is $\sim 1.05 \times$ higher than that of the baseline design. However, the increased fill factor also leads to a significantly larger beam solid angle, making the system more susceptible to background noise.

The average array efficiencies for the three PRIMA use cases, as discussed in Sec. 5, are compared in Fig. 9(c). A significant improvement is observed, particularly for the spectrometer and imaging scenarios, which benefit the most from an increased fill factor when sampling the array sparsely. The average array efficiency increases by $\sim 1.18\times$ for the spectrometer case and $1.28\times$ for the imaging scenario. For a detector noise–limited system, the observing speed grows with the square of array efficiency. The improvement factor due to the increased array efficiency is also summarized in Table 1.

The background noise–limited observing speed is presented in Fig. 9(e). The observing speed remains relative to the same reference case, allowing a direct comparison with the observing speed of circular lenses. When observing an aligned point source, there is no advantage to utilizing the hexagonal corners for sparse sampling $(d_f > 1.4 f_\#^{\text{refl}} \lambda_{0c})$ because the aperture efficiency does not improve significantly while the background noise throughput increases rapidly. It is worth noting that the optimal sampling configuration, which maximizes the observing speed of an aligned point source, corresponds to the crossover point of the aperture efficiency and focusing efficiency shown in Fig. 9(a). This crossover shifts from $d_f = 1.6 f_\#^{\text{refl}} \lambda_{0c}$ to $d_f = 1.4 f_\#^{\text{refl}} \lambda_{0c}$ when utilizing a 100% fill factor array. However, this trend does not hold for the spectrometer or imaging scenarios, where the point source is not necessarily aligned. In these cases, the hexagonal corners contribute to increased observing speed even for sparse sampling, as summarized in Table 1. The observing speed remains maximized for tightly sampled arrays with $d_f < 1 f_\#^{\text{refl}} \lambda_{0c}$.

bChanging the fill factor and absorber size affects the resolution.

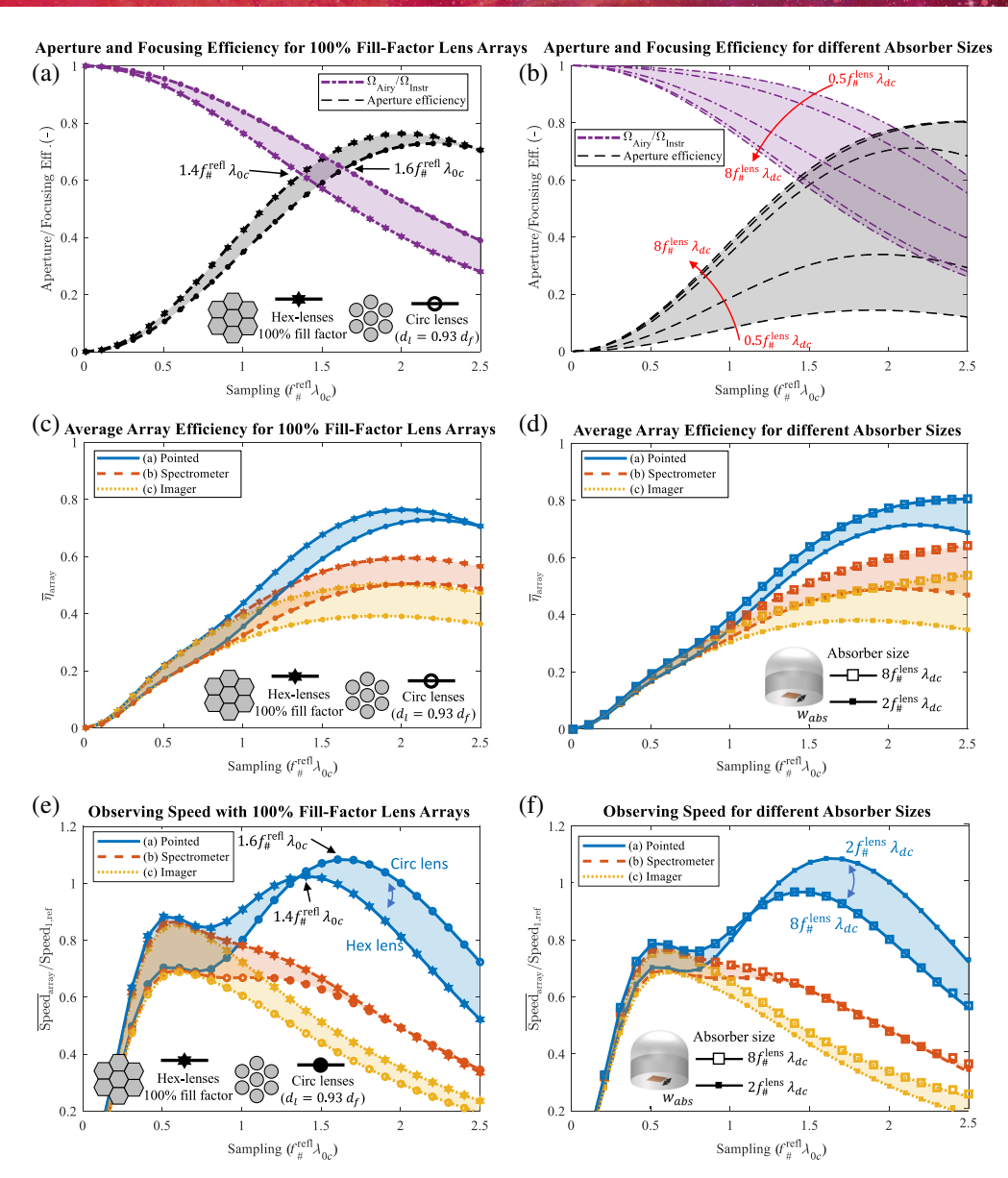


Fig. 9 Study of the effect of microlens fill factor and absorber size in terms of (a) and (b) aperture and focusing efficiency, (c) and (d) average array efficiency for different PRIMA use cases, and (e) and (f) average observing speed for different PRIMA use cases in a background noise–limited scenario. The left column examines the effect of the fill factor, whereas the right column explores the impact of absorber size. Results are shown for the sampling wavelength λ_{0c} .

6.2 Effect of Absorber Size

We now analyze the effect of absorber size across the different PRIMA use cases. The results are summarized in Figs. 9(b), 9(d), and 9(f). The aperture efficiency and focusing efficiency are evaluated for absorber sizes of $w_{abs} = [0.5, 1, 2, 4, 8] f_{\#}^{lens} \lambda_{dc}$. Aperture efficiency declines significantly for absorbers smaller than $w_{abs} < 2f_{\#}^{lens} \lambda_{dc}$, whereas the beam solid angle increases substantially for absorbers larger than $w_{abs} > 1f_{\#}^{lens} \lambda_{dc}$.

The average array efficiency and observing speed in a background noise-limited scenario are shown in Figs. 9(d) and 9(f) for absorber sizes of $w_{abs} = [2,8] f_{\#}^{lens} \lambda_{dc}$. Smaller absorbers are not useful as they exhibit degraded observing speed due to increased spillover losses. For tightly sampled arrays, a larger absorber is beneficial across all PRIMA use cases, as it enhances array efficiency without significantly increasing background noise throughput. This holds true for sparsely sampled arrays in the spectrometer and imaging scenario. When the PSF is misaligned,

power is spread across the lens FP (see Fig. 10), and a larger absorber captures more signal power while introducing minimal additional background noise power. The potential enhancement in relative observing speed is summarized in Table 1. For an aligned point source, the optimal absorber size is approximately $w_{\rm abs} \approx 2 f_{\#}^{\rm lens} \lambda_{dc}$, as it ensures most of the PSF power is captured while minimizing background noise throughput.

7 Optimal Reflector Sampling Configurations

A summary of the optimal reflector focal plane sampling configurations for different PRIMA observing scenarios is shown in Table 1.

In a detector noise–limited system, the observing speed is maximized when the optical efficiency is maximized, as the background noise throughput is negligible compared with detector noise. As shown in Fig. 7, a sparse sampling of $\sim 2.0 f_\#^{\rm refl} \lambda_{0c}$ is optimal for all observing scenarios, with aperture efficiency values between 70 and 73%. However, in the spectrometer and imaging scenarios, where the point source is not necessarily aligned with a pixel, significant power losses occur due to spillover in the reflector focal plane caused by the array fill factor and in the lens focal plane due to under-illumination of the lens. As a result, the average array efficiency decreases to 51% for the spectrometer and 39% for the imaging scenario. Improvements in observing speed can be achieved by increasing the micro-lens array fill factor, leading to a speed gain of up to 1.65×, or by increasing the absorber size or reducing the lens focal number, which results in a speed gain of up to 1.69×.

In a background noise–limited system, the NEP is dominated by sky background noise contributions. A sparsely sampled array results in wider reflector beam patterns, increasing the received background noise. For the pointed mode, the optimal sampling is $1.6f_{\#}^{\rm refl}\lambda_{0c}$, yielding an aperture efficiency of 63%. In this case, increasing the array fill factor or absorber size does not provide a benefit, as any increase in available signal power is offset by the corresponding increase in background noise NEP. For the spectrometer and imaging scenarios, a tightly sampled array with $0.6f_{\#}^{\rm refl}\lambda_{0c}$ periodicity is optimal, as it minimizes power loss when the point source or spectral feature is misaligned with a lens. The system achieves near-diffraction-limited angular resolution. As is expected from any near-Nyquist sampled FPA, see Fig. 2, the aperture efficiency is fundamentally limited to spillover in the reflector focal plane. The aperture efficiency is 15% and can be improved by incoherently summing the power from neighboring pixels. The summed array efficiency, averaged over all relevant pixel phases, is 20%. Further improvements in observing speed can be achieved by increasing the array fill factor, resulting in up to a 1.25× speed gain, or by increasing the relative absorber size, providing up to a 1.15× speed gain.

8 Conclusion

This work presents an analysis of reflector focal plane sampling considerations when using lenscoupled absorbers as focal plane elements for far-infrared imaging and spectroscopy. Although the findings are generalizable, specific case studies are examined in the context of the PRIMA, an astrophysics mission currently under study. An analysis of the fundamental characteristics of lens-coupled absorbers demonstrates that these focal plane elements can be significantly less sensitive to noise from the instrument box and sky background compared with bare absorbers, owing to the focusing effects introduced by the lens. However, this improvement comes at the cost of a reduced aperture efficiency. Using an efficient quasi-analytical approach, we have investigated the optimal focal plane sampling configurations that maximize observing speed across different PRIMA case studies. For detector noise-limited systems and for background noiselimited observations of a point source with a known position, a sparsely sampled array is preferred. Conversely, in general spectrometer applications and 2D mapping scenarios, observing speed is maximized when the focal plane is sampled near the Nyquist rate. In addition, we studied the impact of lens fill factor in the micro-lens array and absorber size. The results indicate that both the lens fill factor and absorber size should be maximized, except in the case of sparsely sampled background noise-limited arrays observing an aligned source, where a more moderate absorber size is preferable.

9 Appendix A: FIRESS's Long-Wavelength Micro-Lens Focal Plane Arrays

The analysis in this work is based on the lens-coupled absorber geometry of the initial prototypes for FIRESS's long-wavelength band, covering a range from $\lambda_{\min} = 0.75\lambda_{c0} = 135~\mu m$ to $\lambda_{\max} = 1.35\lambda_{c0} = 242~\mu m$, with a geometric mean wavelength of $\lambda_{c0} = 180~\mu m$. All four FIRESS bands share an approximate 1:1.8 relative bandwidth. Minimizing the size of the KID absorber/inductor is crucial, as the KID responsivity to incident light scales inversely with the absorber/inductor volume. Optimal absorber sizes in Ref. 6 range from 75 to 105 μm , leading to the selection of fast lenses to achieve a relative absorber size of $w_{abs} \approx 2f_{\#}^{lens}\lambda_{d}$. A relative absorber size of $w_{abs} \geq 2f_{\#}^{lens}\lambda_{d}$ is desired to minimize spillover losses.

Laser ablation technology from Veldlaser Inc. ¹⁸ has demonstrated the capability to fabricate 21×21 lens arrays with moderately low focal numbers of $f_{\#}^{lens} = 1.06$. ¹⁹ Later advancements achieved ultra-low focal numbers of $f_{\#}^{lens} = 0.75$ in the initial characterization of a long-wavelength 21×21 KID array prototype for FIRESS. ⁶ However, large-format (>1k pixels) laser-ablated lens arrays have yet to be demonstrated.

Parallel to these efforts, NASA's GSFC has developed 1008-pixel micro-lens arrays using etching via greyscale lithography. These arrays exhibit excellent surface quality, even for PRIMA's shortest wavelengths down to 24 μ m, and benefit from a rapid manufacturing process. Given their suitability, these micro-lens arrays are now being produced in the PRIMA flight format and serve as the baseline for this study.

The circular lenses are designed with a nominal 900 μ m diameter and a surface profile approximated by an elliptical lens with a focal number of $f_{\#}^{\rm lens}=0.96$. The fabricated lenses (Fig. 3 in Ref. 12) exhibit deviations from the designed profile near the edges, effectively yielding a clear aperture diameter of $0.93d_f=838~\mu$ m. The model used in this paper incorporates this adjusted fabricated lens profile. The geometrical parameters of the lens are summarized in Table 2.

A method for producing single-layer Parylene C AR coatings with multiple thicknesses across a single array has been developed at GSFC using a shadow mask and oxygen plasma etching approach. The AR coating permittivity is assumed to be $\epsilon_r = 2.62$, and the coating thickness is optimized for two wavelength ranges: $\lambda_{\rm ML} = 161~\mu{\rm m}$ (for pixels operating at $\lambda < \lambda_{\rm ML}^{\rm sep}$) and $\lambda_{\rm ML} = 215~\mu{\rm m}$ (for $\lambda \ge \lambda_{\rm ML}^{\rm sep}$), where the separation wavelength is defined as $\lambda_{\rm ML}^{\rm sep} = 188~\mu{\rm m}$.

Table 2 System parameters used in the analysis.

Parameter	Symbol	Value
Absolute reflector FP sampling	d _f	900 μm (fixed)
Reflector focal number	f ^{refl}	Variable depends on relative FP sampling
Nominal lens focal number	$f_\#^{lens}$	0.96
Clear lens diameter	d_I	838 μm
Lens refractive index	nlens	3.42
Sampling wavelength in vacuum	λ_{0c}	180 μm
Sampling wavelength in dielectric	λ_{dc}	53 μ m
Normalized absorber side length	$w_{ m abs}$	$2.08f_\#^{\mathrm{lens}}\lambda_{dc}~(2\lambda_{dc})$
Absolute absorber side length	$w_{ m abs}$	105 μm
AR coating refractive index	n^{AR}	$\sqrt{2.62}$
AR coating thickness (λ_0 < 188 μ m)	t ^{AR}	25 μm
AR coating thickness ($\lambda_0 \ge 188 \ \mu \text{m}$)	t ^{AR}	33 μm

10 Appendix B: Quasi-Analytical Electromagnetic (EM) Model, Validation, and Reference Case

10.1 Quasi-Analytical EM Model

This study employs an efficient FO-based model, following the theoretical framework presented in Refs. 10, 13, and 14. In this quasi-analytical model, the field radiated from a distant point source is incident on an on-axis parabolic reflector. The incident field is modeled as a single-polarized plane wave arriving from the spherical source coordinates θ_s , ϕ_s , as seen from the reflector normal $-\hat{z}$. A schematic representation of the model is shown in the top left panel of Fig. 10.

Using geometrical optics (GO) techniques, the field is propagated to an equivalent FO sphere centered around the reflector focal point, which can be calculated analytically as shown in Ref. 13. The GO field on the equivalent FO sphere is then related to a plane wave spectrum (PWS) representation of the direct field in the reflector FP. This direct field is computed using the FO integral described in Eqs. (3)–(5) of Ref. 10. The reflector FP consists of a hexagonally packed silicon lens array (refractive index $n^{\text{lens}} = 3.42$), as described in Appendix A. The system parameters are summarized in Table 2.

The lens vertex is aligned with the reflector FP (as depicted in Fig. 10), and the reflector's direct field is propagated along the $-\hat{z}$ -direction toward the elliptical lens surface. The field then traverses the AR coating and reaches the equivalent lens FO sphere, using the GO techniques outlined in Ref. 13. This computationally efficient method is valid for moderately large reflector focal numbers ($f_{\#}^{\text{refl}} \gtrsim 2$), which is the case in this study. For lower focal numbers, a coherent FO approach as presented in Ref. 14 can be used, where each plane wave contribution of the reflector PWS is individually propagated toward the lens FO sphere before summing all contributions.

The Fresnel transmission and reflection coefficients of the AR coating are calculated using a transmission line model.^{20,21} The GO field on the lens FO sphere is subsequently used to define a PWS representation of the direct field in the lens FP, $\vec{e}_{\rm fp}^d(x,y)$, which can be efficiently computed using Eq. (3) in Ref. 10.

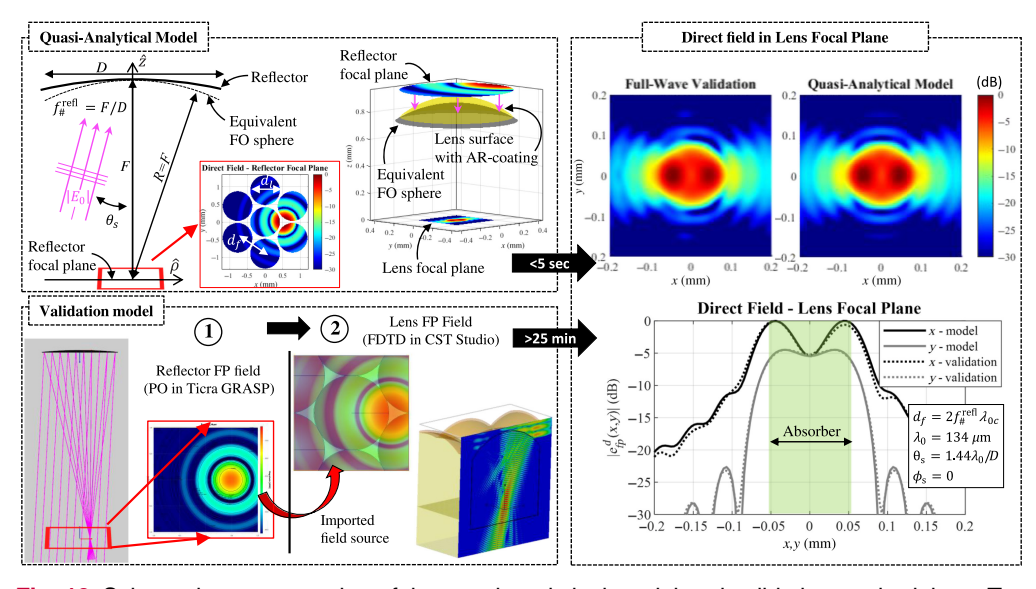


Fig. 10 Schematic representation of the quasi-analytical model and validation methodology. Top left: the model employs a Fourier optics approach to efficiently compute the direct field in the lens FP within seconds. Bottom left: the validation process consists of two steps—first, the direct field in the reflector FP is simulated using PO in TICRA GRASP, and then imported into the full-wave EM-simulator CST Microwave Studio. The FDTD simulation takes over 25 min. Right: comparison of the normalized direct field in the lens FP between the quasi-analytical model and the full-wave simulation. Shown are the fields resulting from a point source located at $\theta_s = 1.44\lambda_0/D$ at 134 μ m for the reference sampling case considered in this study. This field is used to generate the cross symbol in Fig. 11(b).

The effective area of the reflector, $A_i^{\rm eff}(\lambda_0, \theta_s, \phi_s)$, due to an incident plane wave coming from a direction θ_s, ϕ_s can be calculated as

$$A_i^{\text{eff}}(\lambda_0, \theta_s, \phi_s) = \frac{P_{\text{abs},i}}{S_{\text{inc}}},\tag{9}$$

where $P_{abs,i}$ represents the power geometrically available to the absorber of the *i*'th pixel, given by

$$P_{\text{abs},i} = \frac{1}{2\zeta_d} \iint_{W_{\text{abs}}} |\vec{e}_{\text{fp}}^d(x - x_i, y - y_i)|^2 dx dy,$$
 (10)

and S_{inc} is the power density of the incident plane wave with amplitude E_0

$$S_{\rm inc} = \frac{|E_0|^2}{2\zeta_0},$$
 (11)

where ζ_0 and ζ_d denote the wave impedance in air and the lens dielectric medium, respectively. Subsequently, the coupling efficiency of the reflector with aperture area A_{refl} to the plane wave, $\eta_{\text{co},i}(\lambda_0, \theta_s, \phi_s)$, can be calculated as

$$\eta_{\text{co},i}(\lambda_0, \theta_s, \phi_s) = \frac{A_i^{\text{eff}}(\lambda_0, \theta_s, \phi_s)}{A_{\text{refl}}}.$$
(12)

The coupling efficiency can be decomposed into the reflector aperture efficiency, $\eta_{\rm ap}(\lambda_0)$, and the normalized angular response pattern $F_i(\lambda_0, \theta_s, \phi_s)$

$$\eta_{\text{co},i}(\lambda_0, \theta_s, \phi_s) = \eta_{\text{ap}}(\lambda_0) F_i(\lambda_0, \theta_s, \phi_s). \tag{13}$$

Here, the aperture efficiency is defined as the coupling efficiency for a point source aligned with the pixel, whereas the normalized angular response pattern represents the on-sky reflector beam pattern, quantifying the change in coupling efficiency due to a misaligned point source. The aperture efficiency, assumed to be uniform across all pixels in the FPA, accounts for spillover losses in both the reflector FP and lens FP, as well as reflection losses at the lens interface.

The formulation in Ref. 10 can accommodate the specific properties of the absorber itself. However, to maintain generality and ensure independence from absorber geometry, the study focuses on the power geometrically available to the absorber rather than explicitly modeling its detailed absorption characteristics.

10.2 Validation of the Model Using the Reference Configuration

The quasi-analytical model is validated through simulations in commercial solvers, following the approach shown in the bottom left panel of Fig. 10. The configuration used for validation consists of a reflector with $f_{\#}^{\rm refl}=2.5$, corresponding to a sampling periodicity of $d_f=2f_{\#}^{\rm refl}\lambda_{0c}$. This configuration serves as the benchmark case for the relative observing speed analysis presented in Secs. 4–7.

The modeled aperture efficiency is shown in Fig. 11(a), where the impact of different AR coating thicknesses is analyzed. A single AR thickness optimized for the sampling wavelength $\lambda_{0c} = 180 \ \mu \text{m}$ results in a 3 to 7% reduction in aperture efficiency at the band edges compared with a gradient thickness AR coating. In the gradient AR case, each frequency point is simulated using an AR thickness exactly equal to a quarter-wavelength at that frequency. By employing a single-layer dual-thickness AR coating, as described in Appendix A, the aperture efficiency reduction at the band edges is limited to only 1 to 3%.

The normalized angular response pattern is shown in Fig. 11(b) for the sampling wavelength and the band edges. The angle θ_s is normalized to the diffraction-limited half-power beamwidth, λ_0/D . It can be observed that the aperture efficiency increases for decreasing wavelength, whereas the system also becomes more sensitive to off-axis point sources. This effect arises due to two main factors: (1) The beam waist of the PSF in the reflector FP decreases at shorter wavelengths, allowing more power to couple into the clear lens aperture. (2) The beam waist of the PSF in the lens FP also decreases, improving coupling to the small absorber. However, for

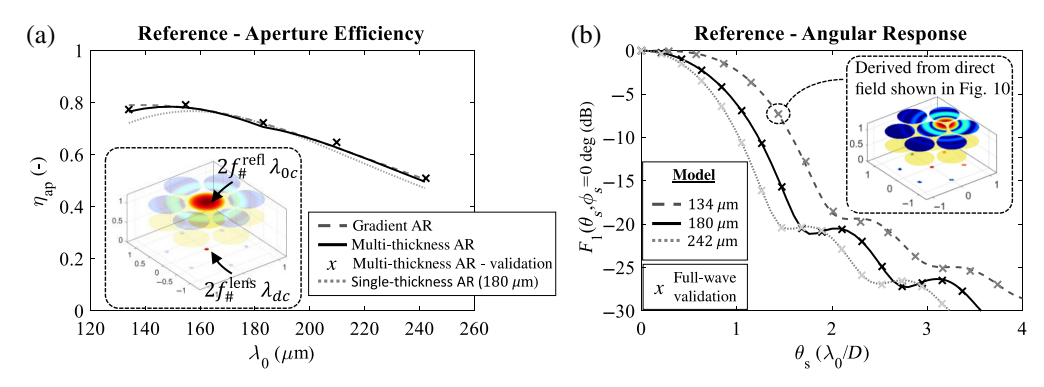


Fig. 11 Validation of the quasi-analytical model for the reference case used in observing speed ratio studies. The case consists of a $2f_{\#}^{\text{refl}}\lambda_{0c}$ -sampled lens with a $2f_{\#}^{\text{lens}}\lambda_{dc}$ perfect square absorber ($\lambda_{0c}=180~\mu\text{m}$). (a) Aperture efficiency for an aligned point source, considering different anti-reflection coatings. (b) Normalized angular response pattern of the on-sky reflector beams. The solid, dashed, and dotted lines represent the quasi-analytical model, whereas the crosses (x) indicate validation using full-wave simulations.

wavelengths shorter than 150 μ m, the aperture efficiency starts decreasing due to underillumination of the lens and the AR coating thickness becoming suboptimal.

Each of the crosses in Fig. 11 represents a validation point obtained using commercial solvers. The validation process consists of three steps: (1) The physical optics (PO) solver in TICRA GRASP is used to simulate the direct field in the reflector FP. (2) This field is then imported at the lens vertex as a field source in the full-wave EM solver CST Microwave Studio. (3) A finite-difference time-domain (FDTD) simulation is performed to compute the direct field in the lens FP. Finally, the fields are numerically integrated (10) to calculate the power geometrically available to the absorber, yielding the coupling efficiency using (12).

For an aligned point source, the resulting coupling efficiency directly corresponds to the aperture efficiency in (13). For misaligned point sources, the aperture efficiency is de-embedded to compute the normalized angular response pattern. The modeled aperture efficiency is consistently 1 to 2% lower than that obtained from commercial solvers, whereas the normalized angular response pattern remains highly accurate beyond the -30-dB level. The modeled and simulated direct fields in the lens FP at $\lambda_0=134~\mu\mathrm{m}$ and a point-source angle of $\theta_s=1.44\lambda_0/D$, corresponding to the cross marker in Fig. 11(b), are shown on the right-hand side of Fig. 10. The comparison demonstrates excellent agreement between the quasi-analytical model and full-wave simulations.

It is worth noting that the computational cost of the quasi-analytical model is less than 5 s per simulation, whereas each validation point using FDTD simulations requires \sim 25 min. In addition, the FDTD-based validation process demands significantly more manual effort to transfer the reflector FP field from the PO solver to the full-wave EM solver. Both the quasi-analytical code and full-wave simulations were executed on a workstation equipped with an Intel Xeon Gold 6230R CPU @ 2.1 GHz and 256 GB RAM.

11 Appendix C: Signal-to-Noise Ratio for Point Sources

The SNR for pixel i is given by

$$SNR_i = \frac{P_i^{\text{sig}}}{\text{NEP}_i} \sqrt{2\tau_{\text{int}}},\tag{14}$$

where P_i^{sig} is the signal power received by the pixel, NEP_i is the total NEP of the pixel, and τ_{int} is the integration time of the detected signal. The total NEP is expressed as an incoherent quadrature sum of the detector noise, NEP_{det}, associated with the detector and readout, and the photon noise, NEP_{ph,i}, which arises from statistical fluctuations in photon arrival

$$NEP_i^2 = NEP_{det}^2 + NEP_{ph,i}^2.$$
 (15)

We assume that the detector noise is uniform across all pixels. The photon noise is given by²²

$$NEP_{ph,i}^2 = \int_{\Delta\nu_{RE}} p_{abs,i}^{tot}(\nu) 2h\nu d\nu, \qquad (16)$$

where h is Planck's constant, $p_{\text{abs},i}^{\text{tot}}(\nu)$ is the total spectral power absorbed by the pixel at frequency $\nu = c_0/\lambda_0$, and $\Delta\nu_{\text{RF}}$ is the RF bandwidth of the pixel.

Although KIDs can couple to broad frequency bands,⁴ PRIMA operates in the shot noise regime across all bands of both instruments. Therefore, the frequency dependence in (16) can be approximated by assuming a square bandpass with bandwidth $\Delta\nu_{\rm opt}$ centered at ν_i . This assumption is particularly valid for FIRESS ($R \sim 130$ spectral bins) and the hyperspectral bands of PRIMAger ($R \sim 10$ spectral bins). The total power absorbed by pixel i, $P_{\rm abs,i}^{\rm tot}(\nu_i) = p_{\rm abs}^{\rm tot}(\nu_i)\Delta\nu_{\rm opt}$, consists of three contributions:

- 1. the signal power P_i^{sig} from a point source
- 2. the power radiated by the sky background, P_i^{sky}
- 3. the power emitted by the telescope, P_i^T , with telescope emissivity ϵ_T and temperature T_T .

We neglect any radiation originating within the instrument enclosure, as it is cooled to 1 K and filtered before reaching the FP enclosure, ensuring it remains subdominant to the sky and telescope loading.

11.1 Signal Power

The signal power absorbed by the pixel is given by

$$P_i^{\text{sig}} = \int_{\Delta\nu_{\text{opt}}} \int_{\Omega_S} A_i^{\text{eff}}(\nu, \Omega) (1 - \epsilon_T) B_{\text{sig}}(\nu, \Omega) d\Omega d\nu, \tag{17}$$

where $A_i^{\rm eff}(\nu,\Omega)$ is the spectral angular effective area of the reflector, and $B_{\rm sig}(\nu,\Omega)$ is the spectral radiance of the source. The spectral angular effective area can be rewritten as $A_i^{\rm eff}(\nu,\Omega)=A_{\rm refl}\eta_{{\rm co},i}(\nu,\Omega)$. As, for a point source, the spectral signal brightness is nonzero only at an infinitesimal source solid angle, $\Omega_s\to 0$ (non-zero only at discrete spherical coordinates θ_s,ϕ_s), and applying the narrowband approximation, we obtain

$$P_i^{\text{sig}} = A_{\text{refl}}(1 - \epsilon_T)\eta_{\text{co},i}(\nu_i, \theta_s, \phi_s)B_{\text{sig}}(\nu_i, \theta_s, \phi_s)\Delta\nu_{\text{opt}}.$$
 (18)

For readability, function dependencies on the center frequency (ν_i) and source location (θ_s, ϕ_s) are omitted in the remainder of this discussion.

11.2 Sky Background and Telescope Emission

Following a similar approach, the power absorbed due to the sky background is given by

$$P_i^{\rm sky} = P^{\rm sky} = A_{\rm refl} \Omega_{\rm instr} (1 - \varepsilon_T) \eta_{\rm ap} B_{\rm sky} \Delta \nu_{\rm opt}. \tag{19}$$

Here, it is assumed that the source solid angle of the sky background is much larger than the instrument beam solid angle such that $\int_{\Omega_s} F_i(\Omega) d\Omega \to \Omega_{\text{instr},i}$. The instrument's beam solid angle, and thus the received sky background power, is assumed to be identical for all pixels, $\Omega_{\text{instr}} = \Omega_{\text{instr},i}$. The spectral radiance of the sky background, B_{sky} , is assumed to be independent of solid angle. Similarly, the power received due to telescope emission is

$$P_i^T = P^T = A_{\text{refl}} \Omega_{\text{instr}} \epsilon_T \eta_{\text{ap}} B_T \Delta \nu_{\text{opt}}, \tag{20}$$

where $\epsilon_T B_T$ represents the spectral radiance of the telescope. We assume that $P^{\rm sky} \gg P_i^{\rm sig}$, meaning that the NEP is dominated by sky background noise and, at the longest PRIMA wavelengths, possibly by telescope emission. Consequently, noise is assumed to be uniform across all pixels, NEP_i = NEP, and the total received noise power is

$$P_{\rm abs}^{\rm tot} = A_{\rm refl} \Omega_{\rm instr} \eta_{\rm ap} B_{\rm ext} \Delta \nu_{\rm opt}, \tag{21a}$$

$$B_{\text{ext}} = (1 - \epsilon_T)B_{\text{sky}} + \epsilon_T B_T. \tag{21b}$$

In Eq. (21b), the spectral radiance contributions from the sky background and telescope are combined into a single external brightness term.

11.3 Signal-to-Noise Ratio

We can now evaluate the SNR for pixel i, observing a point source as

$$SNR_{i} = \frac{A_{\text{refl}}(1 - \epsilon_{T})\eta_{\text{co},i}B_{\text{sig}}\Delta\nu_{\text{opt}}}{\sqrt{NEP_{\text{det}}^{2} + P_{\text{abs}}^{\text{tot}}2h\nu_{i}}}\sqrt{2\tau_{\text{int}}}.$$
(22)

When analyzing a ratio of SNRs, independent parameters will be canceled, which generalizes the study.

12 Appendix D: Signal-to-Noise Ratio When Using Multiple Pixels

The power received by multiple pixels can be combined to improve the SNR.^{8,9} Each pixel acts as an independent estimator of the total power of the PSF incident in the reflector FP, *P*^{PSF}, which can be estimated as

$$P^{\rm PSF} = P_i^{\rm PSF} = \frac{P_i^{\rm sig}}{\eta_{\rm co,i}} = A_{\rm refl} (1 - \epsilon_T) B_{\rm sig} \Delta \nu_{\rm opt}. \tag{23}$$

When combining different independent estimates of the same value, they are weighted by the inverse of the square of their errors, which is given by $(\eta_{co,i}/\text{NEP})^2$. As the NEP is assumed to be identical for all pixels, the weights can be equivalently defined as $\eta_{co,i}^2$. After normalizing by the sum of weights, the total PSF power as estimated by the entire array, $P_{\text{array}}^{\text{PSF}}$, and the incoherently summed array noise power, NEP_{array}, can be expressed in terms of the weighting coefficients, W_i

$$P_{\text{array}}^{\text{PSF}} = \frac{\sum_{i} \eta_{\text{co.}i}^{2} P_{i}^{\text{PSF}}}{\sum_{k} \eta_{\text{co.}k}^{2}} = \sum_{i} W_{i} P_{i}^{\text{sig}}, \tag{24a}$$

$$NEP_{array} = \sqrt{\sum_{i} W_{i}^{2} NEP_{i}^{2}} = NEP \sqrt{\sum_{i} W_{i}^{2}},$$
 (24b)

$$W_i = \frac{\eta_{\text{co},i}}{\sum_k \eta_{\text{co},k}^2}.$$
 (24c)

Finally, the SNR for point source flux extraction using the full array follows:

$$SNR_{array} = \sqrt{\sum_{i} \eta_{co,i}^{2}} \frac{P^{PSF}}{NEP} \sqrt{2\tau_{int}} \equiv \sqrt{\sum_{i} SNR_{i}^{2}}.$$
 (25)

This represents a quadrature summation of the point source coupling efficiencies multiplied by the SNR when the point source coupling efficiency is unity. Equivalently, it can be interpreted as a quadrature sum of the individual pixel SNRs. The relative SNR when observing with the full array, compared with the SNR of the same reference case when observing with a single pixel (i = 1), is then defined as

$$\frac{\text{SNR}_{\text{array}}}{\text{SNR}_{1,\text{ref}}} = \frac{\sqrt{\sum_{i} \eta_{\text{co},i}^{2}}}{\eta_{\text{ap,ref}}} \frac{\text{NEP}_{\text{ref}}}{\text{NEP}}.$$
 (26)

The relative observing speed, $Speed_{array}/Speed_{1,ref}$, follows as the square of the relative SNR given in Eq. (26).

Disclosures

The authors declare that there are no financial interests, commercial affiliations, or other potential conflicts of interest that could have influenced the objectivity of this research or the writing of this paper.

Code and Data Availability

All data and theories used in support of the findings of this paper are available within the article.

Acknowledgments

The research described herein was partly carried out at the Jet Propulsion Laboratory, California Institute of Technology, Pasadena, California, United States, under contract with the National Aeronautics and Space Administration. ©2025 California Institute of Technology. Government sponsorship acknowledged.

References

- 1. A. Moullet et al., "PRIMA general observer science book," arXiv:2310.20572 (2023).
- 2. "PRIMA project website," https://prima.ipac.caltech.edu/ (accessed 19 March 2025).
- M. J. Griffin et al., "The Herschel-SPIRE instrument and its in-flight performance," Astron. Astrophys. 518, L3 (2010).
- P. K. Day et al., "A broadband superconducting detector suitable for use in large arrays," *Nature* 425(6960), 817–821 (2003).
- L. Foote et al., "High-sensitivity kinetic inductance detector arrays for the probe far-infrared mission for astrophysics," J. Low Temp. Phys. 214(3), 219–229 (2024).
- S. Hailey-Dunsheath et al., "Characterization of a far-infrared kinetic inductance detector prototype for PRIMA," arXiv:2311.03586 (2023).
- P. K. Day et al., "A 25-micrometer single-photon-sensitive kinetic inductance detector," *Phys. Rev. X* 14, 041005 (2024).
- 8. T. Naylor, "An optimal extraction algorithm for imaging photometry," *Mon. Not. R. Astron. Soc.* **296**(2), 339–346 (1998).
- M. J. Griffin, J. J. Bock, and W. K. Gear, "Relative performance of filled and feedhorn-coupled focal-plane architectures," *Appl. Opt.* 41(31), 6543–6554 (2002).
- N. Llombart et al., "Reception power pattern of distributed absorbers in focal plane arrays: a Fourier optics analysis," *IEEE Trans. Antenn. Propag.* 66(11), 5990–6002 (2018).
- 11. S. van Berkel et al., "THz imaging using uncooled wideband direct detection focal plane arrays," *IEEE Trans. THz. Sci. Technol.* **7**(5), 481–492 (2017).
- N. F. Cothard et al., "Monolithic silicon microlens arrays for far-infrared astrophysics," Appl. Opt. 63(6), 1481–1487 (2024).
- N. Llombart et al., "Fourier optics for the analysis of distributed absorbers under THz focusing systems," *IEEE Trans. THz. Sci. Technol.* 5(4), 573–583 (2015).
- S. O. Dabironezare et al., "Coherent Fourier optics model for the synthesis of large format lens-based focal plane arrays," *IEEE Trans. Antennas Propag.* 69(2), 734–746 (2020).
- J. Böhm et al., "Cryogenic temperature-dependence of HRFZ silicon refractive index from mid- to far-IR down to 5 K," in 46th Int. Conf. Infrared, Millim. and THz. Waves (IRMMW-THz), pp. 1–2 (2021).
- J. Baselmans et al., "A kilo-pixel imaging system for future space based far-infrared observatories using microwave kinetic inductance detectors," Astron. Astrophys. 601, A89 (2017).
- S. Hailey-Dunsheath et al., "Kinetic inductance detectors for the origins space telescope," J. Astron. Telesc. Instrum. Syst. 7(1), 011015 (2021).
- Veldlaser Inc., "Laser micromachining," https://www.veldlaser.nl/en/laser/micromachining/ (accessed 11 April 2025).
- P. M. Echternach et al., "Large array of single-photon counting quantum capacitance detectors," *IEEE Trans. THz. Sci. Technol.* 12(2), 211–216 (2022).
- 20. H. Zhang, "A GO/FO tool for analyzing quasi-optical systems in reception," (2018).
- 21. H. Zhang et al., "A Fourier optics tool to derive the plane wave spectrum of quasi-optical systems [EM programmer's notebook]," *IEEE Antennas Propag. Mag.* **63**(1), 103–116 (2021).
- 22. P. Richards, "Bolometers for infrared and millimeter waves," J. Appl. Phys. 76(1), 1-24 (1994).

Sven van Berkel is a microwave engineer at NASA's Jet Propulsion Laboratory (JPL), specializing in submillimeter-wave technology for heterodyne and direct detection spectroscopy instruments. He received his PhD in electromagnetics from Delft University of Technology, where he focused on passive THz imaging systems and wideband integrated antenna design. Previously, he was a NASA postdoctoral fellow at JPL. His expertise includes lens-coupled antennas and absorbers, ultrawideband antennas, and quasi-optical system design.

Shahab Oddin Dabironezare received his PhD at TU Delft, the Netherlands, in 2020. From 2020 to 2022, he was a post-doctoral researcher with the Terahertz Sensing Group, TU Delft.

He is currently an assistant professor at TU Delft and an instrument scientist at the Netherlands Institute for Space Research (SRON). His research interests include wideband antennas at (sub)millimeter-wave applications, wide field-of-view imaging systems, quasi-optical systems, lens antennas, and absorber-based detectors.

Goutam Chattopadhyay is a senior scientist at NASA's JPL at the California Institute of Technology (Caltech) and a Visiting Professor at Caltech in Pasadena, United States. He earned his PhD in electrical engineering from Caltech in 2000. He is a fellow of both IEEE (United States) and IETE (India), serves as a track editor for the IEEE Transactions on Antennas and Propagation, and is an IEEE-distinguished lecturer. He is the 2025 president of the IEEE Microwave Theory and Technology Society (MTT-S).

Marc Foote is an instrument system engineer and instrument manager at the Jet Propulsion Laboratory in the Instruments Division. He received his PhD in condensed matter physics from the University of Illinois, Urbana-Champaign. His focus at JPL has involved infrared detector development and flight infrared instruments, as well as the PIXL X-ray spectroscopic mapper for the Perseverance Mars rover.

Jason Glenn is a research astrophysicist in the Observational Cosmology Laboratory at NASA's Goddard Space Flight Center. He is the principal investigator of the PRIMA NASA astrophysical observatory concept. His research interests include star formation, active galactic nuclei, and the interstellar medium in galaxies, and far-infrared through millimeter-wave astrophysical instrumentation and detector development.

Jochem Baselmans is a full professor in experimental astronomy at the Delft University of Technology, a senior instrument scientist at the SRON Netherlands Institute for Space Research, and a member of the global faculty of the University of Cologne. He graduated in 1998 from the University of Groningen and received his PhD (summa cum laude) at the University of Groningen in 2002 studying the superconducting state in normal metal Josephson junctions. He is an expert in microwave kinetic inductance detector technology and related instrumentation for far-infrared astronomy. He invented the concept of the on-chip spectrometer and is the lead system engineer for the first on-chip spectrometer instruments, Deshima (2019) and Deshima-2 (2024). He is the detector lead on the AMKID instrument on the APEX telescope (commissioned in 2025), and he has pushed the sensitivity of MKIDs to a level suitable for operation in cryogenically cooled space-based observatories.

Charles Bradford's research integrates new detector and instrument technology to study the interstellar medium, star formation, and their evolution across cosmic history. He has led the development and fielding of new submillimeter and millimeter-wave spectrometers on mountaintop sites, using the datasets to study gas conditions in galaxies both nearby and distant. A recent thrust has been the development of ultra-sensitive kinetic inductance detector arrays for far-IR astrophysics missions, and he is the project scientist of the PRIMA mission concept.